Full length article

Role of Zr in strengthening MoSi$_2$ from density functional theory calculations

Hui Zheng, Richard Tran, Xiang-Guo Li, Balachandran Radhakrishnan, Shyue Ping Ong[*]

Department of NanoEngineering, University of California San Diego, 9500 Gilman Dr, Mail Code 0448, La Jolla, CA 92093-0448, United States

ABSTRACT

MoSi$_2$ is an important intermetallic with excellent oxidation resistance at high temperatures above 1000 °C. However, its application at lower temperatures is limited by oxygen embrittlement, a phenomenon known as "pesting". In this work, we comprehensively investigate the role of Zr in mitigating pesting in MoSi$_2$ using density functional theory calculations. We show that Zr dopants reduce the embrittling effects of oxygen interstitials at MoSi$_2$ grain boundaries by being a charge donor to oxygen. However, a more substantial effect is observed when Zr is present as a secondary getter nanoparticle phase. Oxygen interstitials have a strong thermodynamic driving force to migrate into the Zr subsurface at the Zr/MoSi$_2$ interface, and the work of separation of the clean and oxygen-contaminated Zr/MoSi$_2$ interfaces are much higher than that of MoSi$_2$ grain boundaries. Finally, we present an efficient screening approach to identify other potential getter elements using simple thermodynamic descriptors, which can be extended to other alloy systems of interest. These findings provide crucial fundamental insights and further avenues to optimize Mo and other alloys.

© 2017 Acta Materialia Inc. Published by Elsevier Ltd. All rights reserved.

1. Introduction

Molybdenum disilicide (MoSi$_2$) is a refractory intermetallic with important high-temperature applications such as heating components, thermal barrier coatings, and turbine engines. This is due to its high melting point (2030 °C) [1,2], moderate density (6.24 g/cm^3) [2] and excellent resistance to oxidation at high temperatures up to 1600 °C due to the formation of a protective coating of SiO$_2$ [2]. However, a major impediment to the widespread application of MoSi$_2$ is its inherent brittleness at intermediate temperatures (~400-600 °C) [3,4]. It has been suggested that the primary cause is grain boundary (GB) embrittlement caused by short-circuit diffusion of O$_2$, a phenomenon known as pesting [2,4].

A common approach to suppress pesting in MoSi$_2$ and other Mo-based intermetallics (such as Mo$_3$Si and Mo$_5$SiB$_2$) is by alloying with "getter" materials, i.e., materials that preferentially react with parasitic oxygen, to improve ductility. These getters commonly exist as nanoparticles embedded in the Mo and Mo-based alloy matrix [5,6]. Examples of ductilizing components include light elements (B, C, Al, Mg) [7–14,31], transition metals (Zr, Ti, V, Nb, Re,

Hf) [6–9,12–17,32], the rare earth metal Er [18] and oxides (La$_2$O$_3$, Y$_2$O$_3$, Sc$_2$O$_3$ and MgAl$_2$O$_4$) [19–22]. In particular, Zr is one of the most commonly used getters that has been shown to efficiently reduce the embrittling effect of O in Mo and Mo-based systems [6–9]. Zr addition increases both ductility and strength in Mo-Si solid solutions and single-phase Mo-1.5Si alloy. Previous experiments on Mo−1.5 at.% Si alloys have attributed these beneficial effects to three reasons [9]. First, Zr addition reduces the grain size of the alloy. Second, Zr reacts with oxygen to form ZrO$_2$ particles, which can pin the GBs. Finally, Zr reduces the concentration of Si segregation at the GB through the formation of ZrSiO$_4$ [1,22,23].

First-principles calculations using density functional theory (DFT) [12,24–27] are an important complementary probe to experiments in studying the effects of dopants/impurities and heterogeneous interface in alloys. For example, Lenchuk et al. have explored the influence of Zr and Si on the strength of pure Mo GBs [27–29]. Their results show that although the presence of Zr and Si results in a lower work of separation in Mo tilt Σ5(310) [001] and twist Σ5 [001] GBs [28], the formation of an ultrathin film of ZrO$_2$ results in a higher work of separation [29]. The embrittling effects of Zr and other impurities in pure Mo GBs have also been studied in a recent comprehensive investigation by Tran et al. [30]. For MoSi$_2$, Waghmare et al. [12] have shown that the substitution of Mo by V or Nb, and substitution of Si by Mg or Al in MoSi$_2$ single crystals can

improve ductility using DFT calculations [12]. We note that these previous studies either focus on just pure Mo metal, or on substitutional dopants in bulk $MoSi_2$; the mechanisms behind the strengthening effects of Zr on the GB and interfaces of Mo-Si alloys remain an important open question.

In this work, we attempt to address this question by comprehensively exploring multiple mechanisms for Zr incorporation into $MoSi_2$ and its interplay with embrittling oxygen contaminants using DFT calculations. We will show that Zr as a dopant has a mitigating effect on oxygen embrittlement at sufficiently high concentrations by acting as a charge donor. We will also show that Zr as a getter nanoparticle significantly enhances the inherent strength of $MoSi_2$ while mitigating the detrimental effects of oxygen impurities. Finally, we will discuss the implications of these findings for the future development of Mo and other alloys, and outline a simple computational approach to screen for other potential getter materials for both Mo and other structural materials using the Materials Project database [33–35].

2. Methods

2.1. DFT calculations

All DFT calculations were performed using the Vienna ab initio Simulation Package (VASP) [36,37] within the projector augmented wave (PAW) approach [38]. The exchange-correlation interactions were modeled using the Perdew-Berke-Ernzerhof (PBE) generalized gradient approximation (GGA) functional [39]. All calculations were spin-polarized, and a plane-wave cutoff energy of 400 eV was used. The energies and atomic forces were converged within 5×10^{-4} eV and 0.02 eV/Å, respectively. Consistent k-point grids of $4 \times 4 \times 1$, $2 \times 2 \times 1$ and $1 \times 1 \times 1$ were used for the 1×1, $\sqrt{2} \times \sqrt{2}$ and 2×2 (scale factors refer to just the GB/interface plane) supercell GB models, respectively. For the α-Zr/$MoSi_2$ and β-Zr/$MoSi_2$ interfaces, gamma-centered k-point grids of $1 \times 1 \times 1$ and $4 \times 4 \times 1$ were used, respectively. All the k-point grids have a density of at least $14/Å^{-1}$ in the GB/interface plane, and convergence tests with respect to both energy cutoff and k-point grid (Fig. S1) show that the work of separation, the main quantity of interest in this work, is converged to within 0.02 J/m². The lattice parameters and atomic positions were fully relaxed for the undoped GB and interface structures, while only the atomic positions were relaxed for the cleaved and doped structures. The construction of all structural models and all analyses were performed using the Python Materials Genomics (pymatgen) library [33].

2.2. Derived quantities

Several quantities are derived from the DFT energy calculations to assess the influence of Zr on the mechanical properties of $MoSi_2$.

Grain boundary/Interface energy. The GB/interface energy $\gamma_{GB/interface}$ is used to determine the most stable grain boundary or interface, and is given by the following expression:

$$\gamma_{GB/interface} = \frac{E_{GB/interface} - \sum_L E_{bulk\ (L)} - \sum_i \Delta n_i \mu_i}{NA_{GB/interface}}$$

where $E_{GB/interface}$ is the energy of the supercell containing the GB/interface; $E_{bulk\ (L)}$ is the energy of the corresponding bulk material L ($MoSi_2$ or Zr); μ_i is the chemical potential of species i; Δn_i is the difference in the number of atoms of species i between the GB/interface supercell and the bulk; N is a normalization constant to account for the number of GB/interface. For a stoichiometric GB/

Table 1
Grain boundary energies (γ_{GB}) and interface energies ($\gamma_{interface}$) with different terminations.

GB	γ_{GB}(J/m²)
Si-Si	2.50
Mo-Mo[a]	2.95
Mo-Si	2.60
Interface (Zr/$MoSi_2$)	$\gamma_{interface}$ (J/m²)
Zr-Si	0.33
Zr-Mo[a]	1.15

[a] non-stoichiometric structure, $\gamma_{GB/interface}$ value corresponds to its lower bound.

interface, $\Delta n_i = 0$ for each species. For non-stoichiometric GB/interfaces, $\sum_i \Delta n_i \mu_i$ is calculated by considering the chemical potential range of interest as outlined by Wei et al. [40], and the corresponding lower bound is listed in Table 1.

Dopant formation energy. The dopant formation energy E_d is used to determine the most favorable site for a particular dopant (O or Zr). The expression for E_d is given as follows:

$$E_d = E_{bulk/GB/interface}^{doped} - E_{bulk/GB/interface}^{pristine} - \sum_i n_i \mu_i$$

where $E_{bulk/GB/interface}^{pristine}$ and $E_{bulk/GB/interface}^{doped}$ are the energies of the clean and doped bulk/GB/interface, respectively. n_i is the number of species i being added ($n_i > 0$) or removed ($n_i < 0$) to form the doped structure, and μ_i is corresponding chemical potential of species i. In this work, μ_i is approximately calculated by the energy per atom of the elemental species i, e.g., solid Zr/Si/Mo and gaseous O_2 to determine dopant site preferences. The energy of gaseous O_2 is obtained via fitting to reproduce the formation energies of main group oxides, in line with the approaches detailed by Wang et al. [41].

Work of separation. The mechanical strength of GBs/interfaces is characterized by the work of separation W_{sep}, which is defined as the energy difference between the cleaved GB/interface ($E_{GB/interface}^{cleaved}$) and the uncleaved GB/interface ($E_{GB/interface}^{uncleaved}$) normalized by the surface area $A_{GB/interface}$ [29], as follows:

$$W_{sep} = \frac{E_{GB/interface}^{cleaved} - E_{GB/interface}^{uncleaved}}{NA_{GB/interface}}$$

Here, N is a normalization constant to account for the number of interfaces cleaved. For the GB structures, a single GB is cleaved by introducing a vacuum layer. For the Zr/$MoSi_2$ interface, two interfaces were cleaved to form four surfaces (see later section).

3. Results

The focus of this work is on the effect of Zr on the strength of oxygen-contaminated $MoSi_2$, both as a dopant in the GBs, as well as a getter nanophase. Two different structural models as shown in Fig. 1, were used to explore these effects. The conventional unit cell of tetragonal $C11_b$ $MoSi_2$ [space group: I4/mmm (No.139)] shown in Fig. 1(a) with fully relaxed DFT lattice parameters of a = 3.220 Å and c = 7.877 Å was used as a fundamental unit in both models. $MoSi_2$ comprises repeating layers of -Si-Mo-Si- atoms. As shown in Table 1, the Si-terminated $MoSi_2$ slab provides the lowest energy $\gamma_{GB/interface}$ for both the GB as well as the Zr/$MoSi_2$ interfaces. All subsequent analysis will henceforth utilize the Si-terminated $MoSi_2$ GB/interfaces.
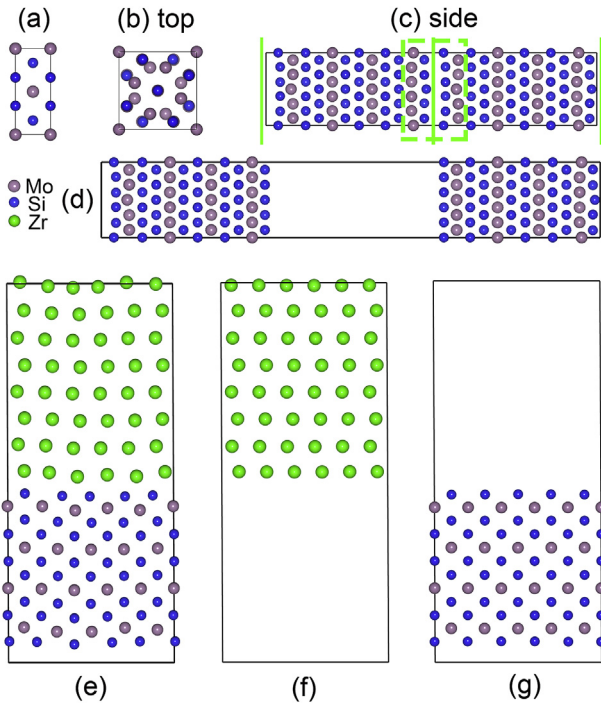
Fig. 1. Models of the clean structures used in this work. (a) Conventional unit cell of tetragonal $C11_b$ $MoSi_2$ (space group: I4/mmm). (b) Top view and (c) side view of the $MoSi_2$ $\Sigma5$ (001) twist grain boundary model, with the green lines illustrating the periodicity of the GB. The sites in the green dashed line box show substitutional and interstitial sites considered. (d) "Cleaved" $MoSi_2$ GB, with a vacuum layer of thickness 15 Å into the GB model. (e) α-Zr/$MoSi_2$ interface model. (f) Zr and (g) $MoSi_2$ slabs obtained after cleaving α-Zr/$MoSi_2$ interfaces. (For interpretation of the references to color in this figure legend, the reader is referred to the Web version of this article.)

3.1. Structural model for MoSi₂ GB

To explore the effect of Zr as a dopant, the $\Sigma5$ (001) twist GB of $MoSi_2$ (henceforth, the term GB in this work is used to refer to this specific GB) was constructed using the coincident site lattice (CSL) model [42], as shown in Fig. 1(b and c). Each model contains two grains forming two equivalent GBs due to periodic boundary conditions. To minimize the interactions between GBs, each grain comprises two unit cells along the direction perpendicular to the GB plane, with approximately 16 Å separating the two GBs. After full relaxation, the lattice parameters of $MoSi_2$ GB are $a = 7.182$ Å and $c = 32.714$ Å.

For doped GBs, equal number of dopants were introduced on both sides of the GB, i.e., both sides of green line within the green dashed line box in Fig. 1(c). It is assumed that any defects introduced is charge-compensated by changes in the Mo or Si oxidation states, i.e., no background charge is applied in the calculations. In all cases, all symmetrically distinct dopant configurations within the 1×1 GB were evaluated, and the lowest energy configuration was used as the basis for analysis. All the configurations and their corresponding energies are provided in the SI. Different impurity coverages were achieved by introducing the same number of dopants into the $\sqrt{2} \times \sqrt{2}$ (240 atoms) and 2×2 (480 atoms) supercells of the GB model from Fig. 1(c) (120 atoms), while ensuring that the distances between dopants are maximized and the local environment around each dopant is similar to that of the relaxed 1×1 cell.

3.2. Site preference of single O and Zr dopant in bulk MoSi₂

To understand the site preference of Zr and O dopants/

Table 2
Dopant formation energy (E_d) of six types of dopant in bulk $MoSi_2$.

| Types of dopant	E_d (eV)
Zr_{Si}	1.98
Zr_{Mo}	1.29
Zr_{int}	7.74
O_{Si}	1.07
O_{Mo}	5.47
O_{int}	0.54

impurities in $MoSi_2$, we first calculated the dopant formation energies for Zr/O substitution on the Mo and Si site (Zr_{Mo}, Zr_{Si}, O_{Mo} and O_{Si} in Kröger−Vink notation) and Zr/O interstitials (Zr_{int}, O_{int}). Table 2 shows the calculated dopant formation energies (E_d) of six types of single dopant in $\sqrt{5} \times \sqrt{5} \times 4$ supercell of bulk $MoSi_2$, which has approximately the same dimensions as the $MoSi_2$ GB model. We find that Zr prefers to substitute on the Mo site rather than the Si site in $MoSi_2$, which is unsurprising given that the atomic radius of Zr (1.55 Å) is much closer to that of Mo (1.45 Å) than Si (1.1 Å). For oxygen impurities, we find that the formation of the oxygen interstitial is much more favorable than substitution on the Si site. This is consistent with previous XPS results showing O signals in the high binding energy region from interstitial oxygen in $MoSi_2$ [43]. O_{int} is also recognized as one of the causes of brittleness of $MoSi_2$-Mo_5Si_3 composite microstructures [18]. In the remainder of this work, we will therefore focus on Zr_{Mo} and O_{int} as the primary defects of interest.

3.3. Zr effect on O embrittlement of MoSi₂ GB

The effects of Zr and O dopants on the strength of the $MoSi_2$ GB were studied by introducing Zr_{Mo} and O_{int} in the $\Sigma5$ (001) twist GB of $MoSi_2$ (Fig. 1(c)). Potential oxygen interstitial sites in the $MoSi_2$ GB were identified using a Voronoi tessellation method [44]. Three dopant compositions were considered:

i Four O_{int}.
ii Two Zr_{Mo}.
iii Four O_{int} and two Zr_{Mo} (one ZrO_2 on each side of the GB).

Fig. 2 summarizes the calculated work of separation W_{sep} for the
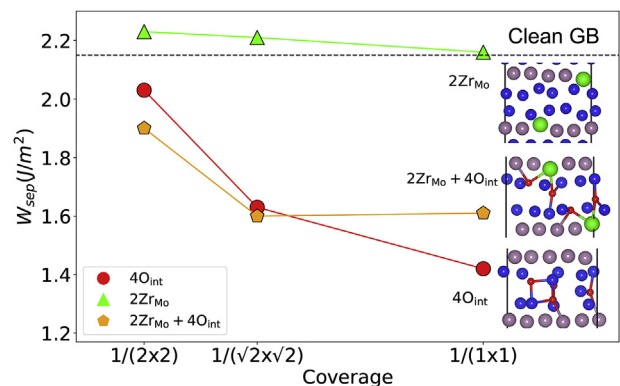
Fig. 2. Work of separation W_{sep} of $\Sigma5$ (001) twist GB of $MoSi_2$ with $4O_{int}$, $2Zr_{Mo}$, and ($4O_{int} + 2Zr_{Mo}$) with respect to coverage (supercell size in the GB plane). The cross-sectional area of the three coverages are 51.6 Å (1×1), 103.0 Å ($\sqrt{2} \times \sqrt{2}$) and 206.3 Å (2×2). Colored lines between points are drawn merely to guide the eyes. The W_{sep} of the clean GB is indicated by the black dashed line. The atomic models for the doped GB for the $1/(1 \times 1)$ coverage are shown. (For interpretation of the references to color in this figure legend, the reader is referred to the Web version of this article.)

clean GB and doped GB with different dopant compositions at three coverages. To calculate W_{sep}, a 15 Å thick vacuum layer was inserted into one of the periodic regions shown by the green line in Fig. 1(c) to generate the "cleaved" model in Fig. 1(d). We have considered all distinct cleavages for each model (see Fig. S2, and Table S1), and plotted the lowest W_{sep} in Fig. 2. We may observe that Zr_{Mo} has a mild strengthening effect on the Σ5 (001) twist GB of MoSi$_2$, though this effect becomes progressively weaker at higher coverages. W_{sep} increases from 2.15 J/m^2 for the clean GB to around 2.16 J/m^2, 2.21 J/m^2 and 2.23 J/m^2 at a coverage of 2 Zr_{Mo} per 51.6 Å^2, 103.0 Å^2, and 206.3 Å^2. Interstitial oxygens, however, have a significant embrittling effect on MoSi$_2$ GBs. W_{sep} drops precipitously by 34% to 1.42 J/m^2 at a high coverage of 4 O_{int} per 51.6 Å^2. As the oxygen coverage decreases, the detrimental effect of oxygen also decreases.

The most interesting result comes from comparing the W_{sep} of the 4 O_{int} + 2 Zr_{Mo} configuration with that of the 4 O_{int} and 2 Zr_{Mo} configurations. We find that even though O_{int} has an embrittling effect on the MoSi$_2$ GB, the W_{sep} of the 4 O_{int} + 2 Zr_{Mo} is higher than that of the 4 O_{int} at high coverages. This result indicates that the presence of Zr in the MoSi$_2$ GB mitigates the severe embrittling effect of the O_{int} at MoSi$_2$ GBs.

3.4. Structural model for Zr/MoSi$_2$ interface

To explore the effect of Zr as a secondary getter nanophase, a Zr/MoSi$_2$ interface model was constructed by interfacing the (0001) surface of α-Zr (hcp) with (001) Si-terminated MoSi$_2$. The pesting effect of MoSi$_2$ that results in formation of MoO$_3$ and SiO$_2$ is the strongest at 500 °C [3,4] where Zr is in its α phase. It should be noted that α-Zr undergoes a phase transition to the β bcc phase at 863°C. [45], which is within the temperature range where problematic formation and evaporation of MoO$_3$ occurs [46]. We have done a similar study using the (110) surface of β-Zr as well, and the results are qualitatively similar. As such, we will focus our discussion on the α-Zr, and the corresponding results for the β phase are available in the Supplementary Information. The α-Zr/MoSi$_2$ model was constructed using a search algorithm to minimize the lattice mismatch while keeping the total number of atoms in the model to around 500 atoms. The resulting model comprises a MoSi$_2$ supercell of 300 atoms interfaced with an α-Zr supercell of 240 atoms (Fig. 1(e)). The lattice mismatch is less than 5% (0.64% along a, 4.58% along b). Several relative shifts of the MoSi$_2$ and Zr supercells were investigated, and the lowest energy configuration was used in subsequent studies. After a full relaxation, the lattice parameters are 16.32 Å, 16.14 Å and 36.91 Å in the a, b and c directions, respectively.

3.5. Relative oxygen affinities of Zr and MoSi$_2$

The relative O affinities of Zr and MoSi$_2$ were probed by inserting a single O_{int} at various symmetrically distinct locations in the Zr/MoSi$_2$ interface model, and performing a DFT relaxation of the atomic positions only. Fig. 3 plots the relative energies (ΔE) of the O_{int}-doped α-Zr/MoSi$_2$ interface against the distance from the interface. The corresponding results for the β-Zr/MoSi$_2$ interface are given in Fig. S3. It is clear that O_{int} has a strong thermodynamic driving force (~6 eV) to move from MoSi$_2$ to Zr. Interestingly, the lowest energy position for the O_{int} is in the subsurface region between the two Zr layers closest to the α-Zr/MoSi$_2$ interface (position 10 in Fig. 3). These results confirm the effectiveness of Zr as a getter for O contaminants in MoSi$_2$. Furthermore, nanoparticles with high surface area to volume ratio would be the most effective getter, consistent with experimental findings [47].

3.6. Mechanical properties of the clean and O-contaminated α-Zr/MoSi$_2$ interface

The W_{sep} of the Zr/MoSi$_2$ interface (Fig. 1(e)) was calculated by cleaving both interfaces to form Zr and MoSi$_2$ slabs (Fig. 1(f)(g)). Similar to the GB study, different cleavages of the Zr/MoSi$_2$ interface were considered (Table S6), and the lowest W_{sep} for the doped and undoped Zr/MoSi$_2$ interfaces are plotted in Fig. 4. We observe that not only do the undoped α-Zr/MoSi$_2$ and β-Zr/MoSi$_2$ interfaces have higher W_{sep} than the clean MoSi$_2$ GB, but the α-Zr/MoSi$_2$ and β-Zr/MoSi$_2$ interfaces contaminated with 4 O_{int} also have substantially higher W_{sep} than the clean MoSi$_2$ GB. In other words, the presence of Zr as a secondary phase not only preferentially absorbs O interstitial contaminants, the Zr/MoSi$_2$ interface, whether oxygen contaminated or not, is also substantially stronger (higher W_{sep}) than MoSi$_2$ GBs. It should also be noted that the observed changes in W_{sep} are much larger in magnitude compared to variations in surface energies as a result of strain (see Table S7).

4. Discussion

From the results above, we have provided clear evidence from first principles calculations of the multiple mechanisms in which Zr mitigates oxygen-caused embrittlement in MoSi$_2$.

4.1. Zr as a dopant

At high coverages, the presence of Zr dopants has a mitigation effect on O-contaminated MoSi2 GBs; the work of separation W_{sep} of the 2 Zr_{Mo} + 4 O_{int} doped GB is higher than that of the 4 O_{int}-doped
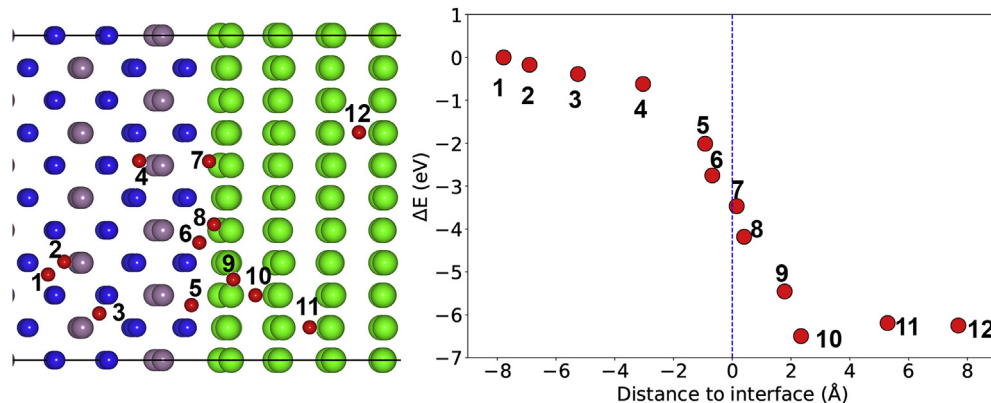

Fig. 3. Relative energies (**ΔE**) of one O_{int} defect at different regions of α-Zr/MoSi$_2$. The zero of the energy is set at the energy of the structure with O_{int} in bulk-like MoSi$_2$ (position 1).
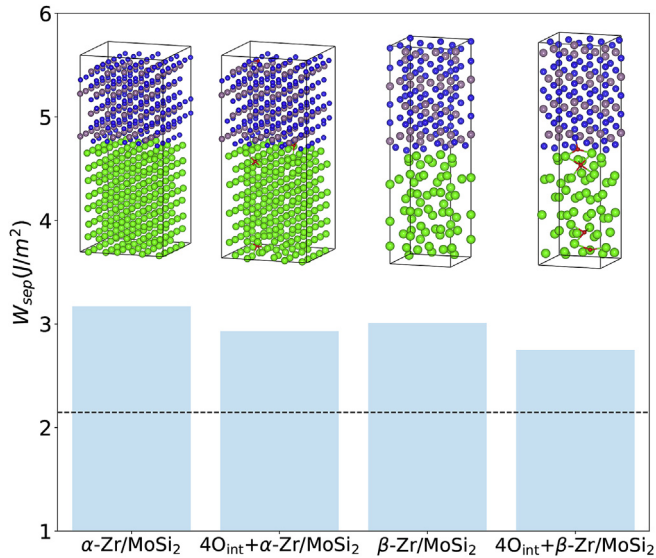
Fig. 4. Work of separation (W_{sep}) of clean and O_{int}-contaminated Zr/MoSi$_2$ interfaces. The black dashed line indicates the W_{sep} of the clean $\Sigma 5$ (001) twist GB of MoSi$_2$ as a reference.
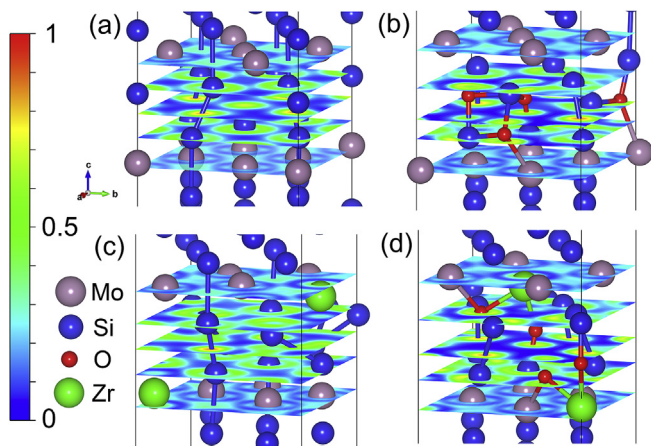

Fig. 5. Electron localization function (ELF) distribution of (a) clean MoSi$_2$ grain boundary (GB), (b) **4O$_{int}$** doped GB, (c) **2Zr$_{Mo}$** doped GB and (d) **4O$_{int}$ + 2Zr$_{Mo}$** doped GB.

GB. We performed electron localization function (ELF) and Bader analysis to reveal how charges transfer between different elements upon the introduction of O_{int} and Zr_{Mo} dopants in MoSi$_2$ (see Fig. 5). Bonding in MoSi$_2$ is known to have hybrid metallic and covalent character [12]. The ELF plots show that electrons in the MoSi$_2$ GB are highly localized (covalent-like) between out-of-plane Si-Si bonds at the clean GB (ELF: yellow). O_{int} introduced into the GB attracts electrons (due to the higher electronegativity of O), resulting in electrons being localized around the O atoms (ELF: orange to red) and a weakening of the covalent bonding between out-of-plane Si. We speculate that this effect causes a reduction in the strength (embrittlement) of the MoSi$_2$ GB. Conversely, the introduction of Zr_{Mo} replaces Mo with a more electropositive element Zr, which donates electrons to O_{int} and mitigates the embrittling effect of O_{int}. These qualitative observations are supported by Bader analysis (Tables S2—S5, Figs. S4—S7), which show similar trends in charge transfer between dopants and MoSi$_2$.

4.2. Zr as a getter

Our calculations show that Zr has a far more substantial effect on the strength of MoSi$_2$ as a getter compared to as a dopant. We find a strong thermodynamic driving force for O_{int} to migrate from MoSi$_2$ to the Zr subsurface region of the Zr/MoSi$_2$ interface (Fig. 3). Though the W_{sep} of the Zr/MoSi$_2$ interface is slightly reduced with Zr-subsurface O_{int}, it is still higher than that of the MoSi$_2$ GB. The subsurface nature of this getting effect of Zr implies that nanoparticles with high surface area to volume ratio would be most effective as getters. Indeed, these findings are consistent with previous experimental studies [47], which find that the addition of Zr promotes the formation of spherical nano-scale particles (ZrO$_2$, Mo$_2$Zr) that are mainly located at GBs as well as partially within the grains. These nanoparticles tend to pin the GBs, further enhancing the mechanical properties of the alloy [9].

4.3. Screening for getter materials

The effect of Zr as a getter for MoSi$_2$ is due to (i) its higher affinity for oxygen interstitials, and (ii) the interface formed by Zr and MoSi$_2$ having a higher W_{sep} and greater resistance to oxygen embrittlement than MoSi$_2$ alone. These insights provide us with the basis to formulate a strategy to computationally screen for other effective getters for MoSi$_2$.

It is clear that performing similarly detailed first principles studies on all possible getter elements would not be feasible, given the computationally- and human-intensive nature of such calculations. However, we can devise readily available proxy computational and experimental descriptors that would allow for an efficient screening:

- **Oxygen exchange reaction energy.** To estimate the relative oxygen affinity of an element A relative to Mo, we use the computed reaction energy for the following oxygen exchange reaction:

$$MoO_3 + 3x/y\,A \rightarrow 3/y\,A_xO_y + Mo$$
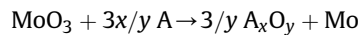
where A_xO_y is the most stable oxide (most negative formation energy) formed by the element A. These reaction energies are computed using pymatgen by querying for the pre-computed data from the Materials Project retrieved via the Materials API [33—35]. The oxygen exchange reaction energy is normalized per MoO$_3$ for comparison across all elements.

- **Silicate formation energy.** A secondary effect of the Zr getter is its ability to decrease glassy SiO$_2$ from the interface via formation of more stable and crystalline silicate ZrSiO$_4$ [1,22] [48]. As a proxy for an element's bonding strength to Si and affinity for silicate formation, we use the lowest formation energy of the $A_xSi_yO_z$ silicate as follows:

$$x\,A + y\,Si + z/2\,O_2 \rightarrow A_xSi_yO_z$$
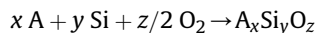
Again, $A_xSi_yO_z$ is chosen to be the most stable A-containing silicate in the Materials Project database. The silicate formation energy is normalized to a per atom basis for comparison across all elements.

- **Melting point.** The getter element should have a relatively high melting point given that the major application of MoSi$_2$ are in high-temperature applications.

Fig. 6 plots the three proxy descriptors for 55 potential element
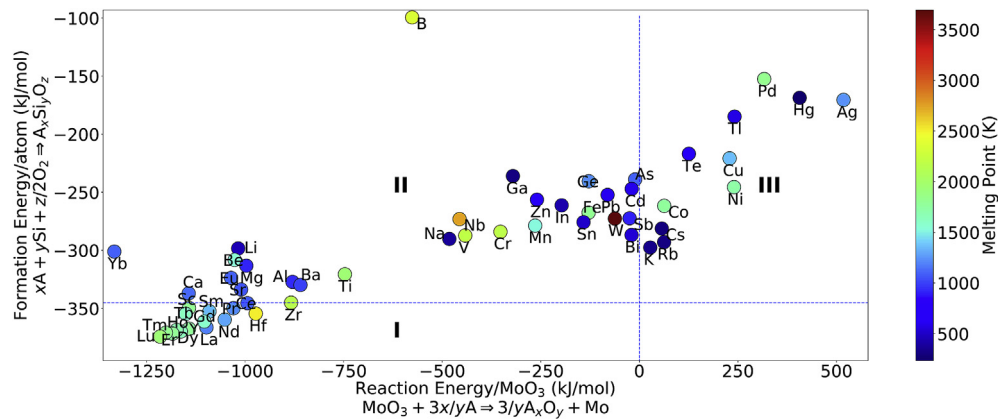
Fig. 6. Plot of silicate formation energy versus oxygen exchange reaction energy for 55 elements in the periodic table. Marker colors represent the melting temperature of each element. A horizontal line is drawn passing through Zr. The regions are labelled as follows: I: oxygen exchange reaction favored and silicate formation energy is lower (more exothermic) than Zr; II: oxygen exchange reaction favored and silicate formation energy is higher (less exothermic) than Zr; III: oxygen exchange reaction not favored but silicate formation energy is negative. (For interpretation of the references to color in this figure legend, the reader is referred to the Web version of this article.)

getters in the periodic table. An ideal getter should be in the bottom left of the plot (region I, i.e., with a negative oxygen exchange reaction energy and a silicate formation energy lower than ZrSiO$_4$) with a high melting point. Elements in region II can still serve as oxygen getters, but silicate formation is less favorable than ZrSiO$_4$. An important validation of our proposed screening strategy is that experimentally well-established strengthening elements such as B, Al, Mg, Zr, Ti, V, Nb, Hf [6–17] mostly lie within regions I and II. Furthermore, the oxides La$_2$O$_3$, Y$_2$O$_3$, Sc$_2$O$_3$ and MgAl$_2$O$_4$ [19–22] are also well-established getters, and all contain elements within regions I and II.

In addition to the known getters, other potential elements in region I are Sc, Y, La, Ce, Pr, Nd, Sm, Gd, Tb, Dy, Ho, Er, Tm, and Lu. Unfortunately, most of these candidates are rare-earth metals with significant supply risks and competing commercial applications. Nonetheless, the more abundant elements such as La and Ce are potentially interesting candidates for further experimental study.

For elements in region II, we will focus on elements with oxygen exchange reaction energies that are more negative, i.e., greater affinity for oxygen, than well-known getters such as Nb and V, which set the upper bound among the known getter materials. Elements in region II satisfying this criterion include Li, Be, Na, Ca, Sr, Ba, Eu, Yb. Among these, Li and Na have too low melting points to be of practical interest. The alkaline-earth metals Ca, Ba and Sr are potentially interesting, though all are relatively soft metals. Ba, in particular, is one of the most well-known getter materials used in vacuum tube applications [49]. Be is another interesting candidate that is expected to outperform Zr in terms of oxygen affinity, though with a slightly less negative silicate formation energy.

It should be noted that there are no silicates in the Materials Project database for the elements Ru, Ta, Re, Au, Ac, Ir, Os, Pt, and Rh, and hence, these are not plotted in Fig. 6. Among these, Ta, Re, and Ac have negative oxygen exchange reaction energies, and therefore are potential oxygen getters. Indeed, Re is well-known ductilizer for Mo [5]. Ta is especially interesting due to its relative abundance and refractory nature.

While we have focused primarily on MoSi$_2$ in this work, the screening approach and descriptors outlined above can be readily adapted to other alloy systems. We note that proper conclusions about the effectiveness of a potential getter need to consider the relative W_{sep} of the oxygen-contaminated interface between the getter and the host, compared to the oxygen-contaminated host GB. Therefore, the above screening process should be considered only as an initial pre-screening for subsequent detailed investigations.

Using the large quantity of pre-computed data in the Materials Project, this rapid screening can significantly narrow down the list of candidates that need to be considered for further first principles (e.g., the GB and interface studies in this work) and experimental studies.

5. Conclusion

To conclude, we have investigated two mechanisms for Zr incorporation into MoSi$_2$ – as a dopant and as a getter secondary phase using density functional theory calculations. We find that though Zr dopants mitigate the embrittling effect of oxygen interstitials in MoSi$_2$ GBs, a far more significant effect is observed when Zr is present as a secondary phase. There is a strong thermodynamic driving force for oxygen interstitials to migrate to the Zr subsurface of the Zr/MoSi$_2$ interface, and the resulting interface has a higher work of separation than MoSi$_2$ GBs. Using simple thermodynamic descriptors, we have also identified other elements that may serve as possible getter materials for MoSi$_2$. These insights pave the way for rational design of MoSi$_2$ and other alloys for improved oxidation resistance.

Appendix A. Supplementary data

Supplementary data related to this article can be found at https://doi.org/10.1016/j.actamat.2017.12.017.

References

[1] Y. Suzuki, T. Sekino, K. Niihara, Effects of ZrO$_2$ addition on microstructure and mechanical properties of MoSi$_2$, Scripta Metall. Mater. 33 (1995) 69–74,

https://doi.org/10.1016/0956-716X(95)00093-B.

[2] Z. Yao, J. Stiglich, T.S. Sudarshan, Molybdenum silicide based materials and their properties, J. Mater. Eng. Perform. 8 (1999) 291–304, https://doi.org/10.1361/105994999770346837.

[3] T.C. Chou, T.G. Nieh, Kinetics of MoSi₂ pest during low-temperature oxidation, J. Mater. Res. 8 (1993) 1605–1610, https://doi.org/10.1557/JMR.1993.1605.

[4] T.C. Chou, T.G. Nieh, Pesting of the high-temperature intermetallic MoSi₂, JOM 45 (1993) 15–21, https://doi.org/10.1007/BF03222509.

[5] J.H. Schneibel, P.F. Tortorelli, R.O. Ritchie, J.J. Kruzic, Optimization of Mo-Si-B intermetallic alloys, Metall. Mater. Trans. 36 (2005) 525–531, https://doi.org/10.1007/s11661-005-0166-4.

[6] J.A. Lemberg, R.O. Ritchie, Mo-Si-B alloys for ultrahigh-temperature structural applications, Adv. Mater. 24 (2012) 3445–3480, https://doi.org/10.1002/adma.201200764.

[7] M.K. Miller, E.A. Kenik, M.S. Mousa, K.F. Russell, A.J. Bryhan, Improvement in the ductility of molybdenum alloys due to grain boundary segregation, Scr. Mercat. 46 (2002) 299–303, https://doi.org/10.1016/S1359-6462(01)01242-8.

[8] M.K. Miller, A.J. Bryhan, Effect of Zr, B and C additions on the ductility of molybdenum, Mater. Sci. Eng. 327 (2002) 80–83, https://doi.org/10.1016/S0921-5093(01)01880-9.

[9] H. Saage, M. Kruger, D. Sturm, M. Heilmaier, J.H. Schneibel, E. George, L. Heatherly, C. Somsen, G. Eggeler, Y. Yang, Ductilization of Mo-Si solid solutions manufactured by powder metallurgy, Acta Mater. 57 (2009) 3895–3901, https://doi.org/10.1016/j.actamat.2009.04.040.

[10] A. Kumar, B.L. Eyre, Grain boundary segregation and intergranular fracture in molybdenum, Proc. R. Soc. A Math. Phys. Eng. Sci. 370 (1980) 431–458, https://doi.org/10.1098/rspa.1980.0043.

[11] P. Peralta, S. a Maloy, F. Chu, J.J. Petrovic, T.E. Mitchell, Mechanical properties of monocrystalline C11b MoSi₂ with small aluminum additions, Scr. Mercat. 37 (1997) 1599–1604, https://doi.org/10.1016/S1359-6462(97)00280-7.

[12] U.V. Waghmare, E. Kaxiras, V.V. Bulatov, M.S. Duesbery, Effects of alloying on the ductility of MoSi₂ single crystals from first-principles calculations, Model. Simulat. Mater. Sci. Eng. 6 (1998) 493–506, https://doi.org/10.1088/0965-0393/6/4/013.

[13] A.A. Sharif, A. Misra, J.J. Petrovic, T.E. Mitchell, Solid solution hardening and softening in MoSi₂ alloys, Scr. Mercat. 44 (2001) 879–884, https://doi.org/10.1016/S1359-6462(00)00698-9.

[14] A.A. Sharif, A. Misra, J.J. Petrovic, T.E. Mitchell, Alloying of MoSi₂ for improved mechanical properties, Intermetallics 9 (2001) 869–873, https://doi.org/10.1016/S0966-9795(01)00084-X.

[15] M. Krüger, D. Schliephake, P. Jain, K.S. Kumar, G. Schumacher, M. Heilmaier, Effects of Zr additions on the microstructure and the mechanical behavior of PM Mo-Si-B alloys, Jom 65 (2013) 301–306, https://doi.org/10.1007/s11837-012-0475-1.

[16] J.J. Petrovic, Toughening strategies for MoSi₂-based high temperature structural silicides, Intermetallics 8 (2000) 1175–1182, https://doi.org/10.1016/S0966-9795(00)00044-3.

[17] C.B. Geller, R.W. Smith, J.E. Hack, P. Saxe, E. Wimmer, A computational search for ductilizing additives to Mo, Scr. Materials 52 (2005) 205–210, https://doi.org/10.1016/j.scriptamat.2004.09.034.

[18] R. Gibala, A.K. Ghosh, D.C. Van Aken, D.J. Srolovitz, A. Basu, H. Chang, D.P. Mason, W. Yang, Mechanical behavior and interface design of MoSi₂-based alloys and composites, Mater. Sci. Eng. 155 (1992) 147–158, https://doi.org/10.1016/0921-5093(92)90322-R.

[19] G. Liu, G.J. Zhang, F. Jiang, X.D. Ding, Y.J. Sun, J. Sun, E. Ma, Nanostructured high-strength molybdenum alloys with unprecedented tensile ductility, Nat. Mater. 12 (2013) 344–350, https://doi.org/10.1038/nmat3544.

[20] I.M. Gunter, J.H. Schneibel, J.J. Kruzic, Ductility and fracture toughness of molybdenum with MgAl₂O₄ additions, Mater. Sci. Eng. 458 (2007) 275–280, https://doi.org/10.1016/j.msea.2006.12.128.

[21] P. Jéhanno, M. Böning, H. Kestler, M. Heilmaier, H. Saage, M. Krüger, Molybdenum alloys for high temperature applications in air, Powder Metall. 51 (2008) 99–102, https://doi.org/10.1179/174329008X313379.

[22] Y. Suzuki, P.E.D. Morgan, K. Niihara, T. Pavelkova, J. Ba, M. Nikl, I. Jakubec, Improvement in mechanical properties of powder-processed MoSi₂ by the addition of Sc₂O₃ and Y₂O₃, J. Am. Ceram. Soc. 81 (1998) 3141–3149, https://doi.org/10.1111/j.1151-2916.1998.tb02749.x.

[23] W.W. Mao, Kinetics of Self-healing Reaction in TBC with MoSi₂ Based Sacrificial Particles, Delft University of Technology, 2013. https://repository.tudelft.nl/islandora/object/uuid:1327ad1b-4638-407b-a801-4baac7b23f27?collection=education.

[24] D.E. Jiang, E.A. Carter, Prediction of strong adhesion at the MoSi₂/Fe interface, Acta Mater. 53 (2005) 4489–4496, https://doi.org/10.1016/j.actamat.2005.06.001.

[25] K.A. Marino, B. Hinnemann, E.A. Carter, Atomic-scale insight and design principles for turbine engine thermal barrier coatings from theory, Proc. Natl. Acad. Sci. U. S. A 108 (2011) 5480–5487, https://doi.org/10.1073/pnas.1102426108.

[26] A. Arya, E.A. Carter, Structure, bonding, and adhesion at the ZrC(1 0 0)/Fe(1 1 0) interface from first principles, Surf. Sci. 560 (2004) 103–120, https://doi.org/10.1016/j.susc.2004.04.022.

[27] O. Lenchuk, J. Rohrer, K. Albe, Solubility of zirconium and silicon in molybdenum studied by first-principles calculations, Scr. Mercat. 97 (2015) 1–4, https://doi.org/10.1016/j.scriptamat.2014.10.007.

[28] O. Lenchuk, J. Rohrer, K. Albe, Atomistic modelling of zirconium and silicon segregation at twist and tilt grain boundaries in molybdenum, J. Mater. Sci. 51 (2016) 1873–1881, https://doi.org/10.1007/s10853-015-9494-y.

[29] O. Lenchuk, J. Rohrer, K. Albe, Cohesive strength of zirconia/molybdenum interfaces and grain boundaries in molybdenum: a comparative study, Acta Mater. 135 (2017) 150–157, https://doi.org/10.1016/j.actamat.2017.05.070.

[30] R. Tran, Z. Xu, N. Zhou, B. Radhakrishnan, J. Luo, S.P. Ong, Computational study of metallic dopant segregation and embrittlement at molybdenum grain boundaries, Acta Mater. 117 (2016) 91–99, https://doi.org/10.1016/j.actamat.2016.07.005.

[31] H. Hu, X. Wu, R. Wang, W. Li, Q. Liu, First principles study on the phase stability and mechanical properties of MoSi₂ alloyed with Al, Mg and Ge, Intermetallics 67 (2015) 26–34, https://doi.org/10.1016/j.intermet.2015.07.008.

[32] S.P. Sun, X.P. Li, Y. Zhang, H.J. Wang, Y. Yu, Y. Jiang, D.Q. Yi, Prediction of the mechanical properties of MoSi₂ doped with Cr, Nb and W from first-principles calculations, J. Alloy. Comp. 714 (2017) 459–466, https://doi.org/10.1016/j.jallcom.2017.04.271.

[33] S.P. Ong, W.D. Richards, A. Jain, G. Hautier, M. Kocher, S. Cholia, D. Gunter, V.L. Chevrier, K.A. Persson, G. Ceder, Python Materials Genomics (pymatgen): a robust, open-source python library for materials analysis, Comput. Mater. Sci. 68 (2013) 314–319, https://doi.org/10.1016/j.commatsci.2012.10.028.

[34] S.P. Ong, S. Cholia, A. Jain, M. Brafman, D. Gunter, G. Ceder, K.A. Persson, The Materials Application Programming Interface (API): a simple, flexible and efficient API for materials data based on REpresentational State Transfer (REST) principles, Comput. Mater. Sci. 97 (2015) 209–215, https://doi.org/10.1016/j.commatsci.2014.10.037.

[35] A. Jain, S.P. Ong, G. Hautier, W. Chen, W.D. Richards, S. Dacek, S. Cholia, D. Gunter, D. Skinner, G. Ceder, K.A. Persson, Commentary: the materials project: a materials genome approach to accelerating materials innovation, Apl. Mater. 1 (2013) 1–11, https://doi.org/10.1063/1.4812323, 011002.

[36] W. Kohn, L.J. Sham, Self-consistent equations including exchange and correlation effects, Phys. Rev. 140 (1965), https://doi.org/10.1103/PhysRev.140.A1133.

[37] G. Kresse, J. Furthmüller, Efficient iterative schemes for ab initio total-energy calculations using a plane-wave basis set, Phys. Rev. B 54 (1996) 11169–11186, https://doi.org/10.1103/PhysRevB.54.11169.

[38] P.E. Blöchl, Projector augmented-wave method, Phys. Rev. B 50 (1994) 17953–17979, https://doi.org/10.1103/PhysRevB.50.17953.

[39] J.P. Perdew, K. Burke, M. Ernzerhof, Generalized gradient approximation made simple, Phys. Rev. Lett. 77 (1996) 3865–3868, https://doi.org/10.1103/PhysRevLett.77.3865.

[40] S.-H. Wei, S.B. Zhang, Chemical trends of defect formation and doping limit in II-VI semiconductors: the case of CdTe, Phys. Rev. B 66 (2002) 155211. https://link.aps.org/doi/10.1103/PhysRevB.66.155211.

[41] L. Wang, T. Maxisch, G. Ceder, Oxidation energies of transition metal oxides within the GGA+U framework, Phys. Rev. B 73 (2006) 195107, https://doi.org/10.1103/PhysRevB.73.195107.

[42] A. Brokman, R.W. Balluffi, Coincidence lattice model for the structure and energy of grain boundaries, Acta Metall. 29 (1981) 1703–1719, https://doi.org/10.1016/0001-6160(81)90005-5.

[43] L. Shaw, R. Abbaschian, Chemical states of the molybdenum disilicide (MoSi₂) surface, J. Mater. Sci. 30 (1995) 5272–5280, https://doi.org/10.1007/BF00356081.

[44] C.B. Barber, D.P. Dobkin, H. Huhdanpaa, The quickhull algorithm for convex hulls, ACM Trans. Math Software 22 (1996) 469–483, https://doi.org/10.1145/235815.235821.

[45] F. Garzarolli, R. Adamson, Microstructure of zirconium alloys and effects on performance, Adv. Nucl. Technol. Int. Eur. AB, ANT Int 2015 (2015), 4–2 (4–8).

[46] D.M. Dimiduk, J.H. Perepezko, Mo-Si-B alloys: developing a revolutionary turbine-engine material, MRS Bull. 28 (2003) 639–645, https://doi.org/10.1557/mrs2003.191.

[47] R. Li, G. Zhang, B. Li, X. Chen, S. Ren, J. Wang, J. Sun, The multi-scale microstructure and strengthening mechanisms of Mo-12Si-8.5BxZr (at.%) alloys, Int. J. Refract. Metals Hard Mater. 68 (2017) 65–74, https://doi.org/10.1016/j.ijrmhm.2017.06.007.

[48] Y. Suzuki, P.E.D. Morgan, K. Niihara, The improvement in mechanical properties of MoSi₂ through in situ crystallization of grain boundary silica glass by the additions of refractory oxides, Mater. Sci. Eng. 261 (1999) 188–195. http://www.sciencedirect.com/science/article/pii/S092150939801065X.

[49] W. Espe, M. Knoll, M.P. Wilder, Getter materials for electron tubes, Vacuum 1 (1951) 128–133, https://doi.org/10.1016/0042-207X(51)90066-8.